# High-throughput, three-dimensional isotropic imaging of whole mouse brain using multi-angle-resolved subvoxel SPIM

Jun Nie[1+], Sa Liu[1+], Tingting Yu[2], Yusha Li[2], Junyu Ping[1], Fang Zhao[1], Yujie Huang[3], Wei Mei[3], Shaoqun Zeng[2], Dan Zhu[2*] and Peng Fei[1,2*]

[1] School of Optical and Electronic Information, Huazhong University of Science and Technology, Wuhan, 430074, China.

[2] Britton Chance Center for Biomedical Photonics, Wuhan National Laboratory for Optoelectronics, Huazhong University of Science and Technology, Wuhan, 430074, China.

[3] Department of Anesthesiology, Tongji Hospital, Tongji Medical College, Huazhong University of Science and Technology, Wuhan, 430030, China

## Abstract

Recent integration of light-sheet microscopy and tissue-clearing has become an important alternative to conventional histology imaging approaches. However, *intoto* cellular mapping of the neural circuits throughout an intact mouse brain remains highly challenging, requiring complicated mechanical stitching and suffering from anisotropic resolution insufficient for high-quality reconstruction in three dimensions. Here we propose the use of a multi-angle-resolved subvoxel selective plane illumination microscope (Mars-SPIM) to achieve high-throughput imaging of whole mouse brain at isotropic cellular resolution. This light-sheet imaging technique can computationally improve the spatial resolution over 6 times under large field of view, eliminating the use of slow tile stitching. Furthermore, it can recover complete structural information

of the sample from thick-tissue scattering/attenuation. With Mars-SPIM, we can readily obtain the digital atlas of a cleared whole mouse brain (~7 by 9.5 by 5 mm) with isotropic resolution of ~2 μm (1 μm voxel) and short acquisition time of 30 minutes. as the mapping of different neuron populations and tracing of long-distance neural projections over the entire brain. Mars-SPIM is thus well suited for high-throughput cell profiling / phenotyping of brain and other mammalian organs.

## Introduction

Comprehensive understanding of complex cellular connections in the whole mammalian brain is one of the fundamental challenges in neuroscience. To unravel the various neuronal profiles of different physiological functions in the whole brain, three-dimensional (3-D), high-resolution imaging is required over a mesoscale large volume[1,2]. However, creating such a large-scale brain dataset has posed big challenge to current 3-D optical microscopy methods, which all show relatively small optical throughputs[3-5]. Furthermore, whether tissue clearing technique is applied or not, light scattering and attenuation remain an outstanding issue that limits the extraction of signals from the deep of brain. To address these issues, 3-D tile stitching combined with brain sectioning has been a popular strategy for obtaining mammalian brain atlases, which can be a meaningful platform for mapping neuronal populations, activities, or connections over the entire brain[6]. For example, sequential two-photon (STP) microscopy can three-dimensionally image the brain at subcellular high resolution[7-15], but at the cost of long-time acquisition up to several days and high-maintaining system

setup. The advent of light-sheet fluorescence microscopy[16-22] (LSFM) in conjunction with tissue-clearing[23-25] eliminates the need of complicated mechanical slicing of the samples by applying a nondestructive optical sectioning instead. At the same time, although LSFM still needs the repetitive image stitching to achieve high lateral resolution over large field of view (FOV), its use of wide-field detection shows higher imaging speed as compared to point-by-point scan in epifluorescence methods. A few well-known designations in LSFM, for example, selective plane illumination microscopy (SPIM) has been recently used for mouse brain imaging with balanced speed and spatial resolution. However, the axial extent of plane illumination in SPIM has to be compromised to its lateral illumination FOV so that an anisotropic axial resolution, typically at 5 to 20 μm depending on the size of the mosaic patch need to be illuminated, is yielded for whole-brain scale imaging[26,27]. As a result, the fine neuronal structures and connections are difficult to be resolved in three dimensions, as what have been achieved by conventional epifluorescence methods, such as micro-optical sectioning tomography[13,14] (MOST) and STP excitation microscopy[10-12]. Furthermore, even with much larger imaging depth enabled by tissue clearing[27-30], photon absorption and scattering of the clarified tissues, still exist in whole mammalian organs. They cause the noticeable deterioration of signals from the deep of tissues. Recently, the multi-view fusion techniques[31-33] which have been previously used in the imaging of small live embryos[34,35] are also applied to the excised mouse brains. It improves the relatively low axial resolution and suppresses the deep tissue scattering[36]. However, for the direct imaging of mesoscale intact organs, the lateral resolution of SPIM system, 5 μm at its

best, is already insufficient to visualize single cells under a large FOV of over 5 mm. In such circumstance, multi-view techniques can't overcome the lateral resolution limit determined by the detection optics. On the other hand, its possible combination with repetitive image stitching will significantly reduce the throughput advantage of LSFM as well as photon utility.

Here we present a whole-brain mapping pipeline, termed multi-angle-resolved subvoxel SPIM (Mars-SPIM), that can image the whole mouse brain at isotropic voxel resolution of ~1 μm and high throughput of half an hour per brain. This imaging strategy combines our sub-voxel-resolving computation[37] with multi-view Bayesian deconvolution[33,38] to achieve fast and accurate reconstruction of whole brain with isotropic super-resolution. Unlike conventional whole-brain imaging methods that use stepwise z-scan and 3-D tile stitching, Mars-SPIM directly records low-resolution whole-brain images using a continuous, non-axial scanning method. This unique scanning mode provides a high acquisition rate, and meanwhile encrypts sub-resolution shifts into raw images. After obtaining these spatially modulated images under four to eight views, all the views are first processed by a MLE-based (maximum likelihood estimation) sub-voxel-resolving (SVR) computation to increase resolution. Then a neuron-feature-based registration followed by a multi-view Bayesian deconvolution (MVD) are applied to generate a final output with showing isotropic super-resolution as well as complete whole-brain structural information. In addition, this computation pipeline is parallelized with multi-GPUs acceleration, achieving a high reconstruction throughput (gigavoxels per minute) matched with the fast data acquisition. With

reconstructing single-cell-resolution whole-brain atlas, we demonstrate successful brain-wide tracing of single neural projections and counting of different neuronal populations over the entire brain. Mars-SPIM shows superior spatial-temporal performance for large-scale cell profiling, in which sample size, spatial resolution and imaging throughput are all highly valued. It's thus suitable for system-level cellular analysis of brain or other whole organs.

## Results

### Mars-SPIM setup and characterization

We develop a Mars-SPIM system, which has a low-profile setup with wide-FOV illumination and detection that cover the entire mouse brain (see Methods and Supplementary Figure 1 and 2). Under a certain view, the brain sample was continuously scanned across the laser-sheet along a non-axial direction. The camera was synchronized to sequentially record a stack of plane images with step-size significantly smaller than the laser-sheet thickness. This non-axial scanning mode of Mars-SPIM encoded the low-resolution (LR) raw image stack with sub-voxel spatial shifts, which were used to reconstruct high-resolution (HR) images through applying a SVR algorithm (Supplementary Figure 3). The sample was then rotated along y axis and non-axially imaged under multiple views (Figure 1a). After the SVR computation generating a series of HR images, anisotropic volumes for all the views, a neuron feature-based registration followed by a multi-view Bayesian deconvolution (MVD) was then applied to accurately align the multiple SVR volumes, compute their

113 conditional probability and finally produce an output with recovering complete signals
114 and presenting isotropic super-resolution in three dimensions. This SVR-MVD fused
115 computation pipeline is further illustrated in Figure 1b and Supplementary Figure 3.

116 We used fluorescent microbeads with ~500 nm diameter as point source to
117 characterize the Mars-SPIM system (Figure 1c and Supplementary Figure 4). For each
118 view, the microbeads were scanned by a ~12 μm thick (full width at half maximum
119 value, FWHM) laser-sheet with 280 nm step-size and detected by a 4×/0.16 objective.
120 This non-axial scanning process (10 degrees to x-z and y-z plane) generated a sub-
121 resolution shift of 48 and 272 nm in lateral and axial directions, respectively. Thirty-
122 four groups of LR image volumes that represented the standard resolution of system
123 optics (voxel size: 1.625 by 1.625 by 4.5 μm) were extracted from raw image sequence
124 to compute the HR images. The raw LR, single-view SVR, conventional MVD and
125 SVR-MVD results are compared in Figure 1c. The line intensity profiles of the resolved
126 beads are plotted in Figure 1d and e, to indicate the lateral and axial resolutions of these
127 methods. The achievable lateral and axial FWHMs of SVR-MVD are improved from
128 ~4.2 μm and 12 μm of the raw image to isotropic ~1.4 μm, which are superior to either
129 single-view SVR (1.7 μm and 4.5 μm) or conventional MVD (isotropic 3.4 μm).

130 We then demonstrate the imaging capability of Mars-SPIM using a clarified brain
131 tissue of transgenic mouse (*thy1-GFP-M*). The brain sample was optically sectioned by
132 a 15 μm laser-sheet and imaged by a 4×/0.28 objective plus a high-speed camera
133 (Hamamatsu Flash 4.0 v2) at a rate of 50 fps. The brain sample was translated with a
134 non-axial step-size of 280 nm (4*4*2 enhancement) and rotated 45 degrees for each

135 new view. Eight view image stacks were rapidly recorded in totally ~20 minutes. The
136 raw image volume of each view simply accepted the limited resolution from the system
137 optics, hence the densely-packed neuronal fibers remained unresolvable (Figure 2a).
138 SVR procedure for each view then started with an initial guess which was simply a ×4
139 interpolation of one of the subdivided LR group, and iteratively converged to the HR
140 solution (data not shown). Then in multi-view registration step, the neuronal cell bodies
141 were recognized as features to establish correspondences instead of beads. This cell-
142 based registration is verified to be as accurate as the bead-based one (Supplementary
143 Figure S5 and 6), and produce a cleaner visualization at the same time (Supplementary
144 Video1 and 2). Figure 2c shows the final Mars-SPIM result with reconstructed voxel
145 size of 0.4 μm. This result is furthermore compared to conventional multiview SPIM
146 (Mv-SPIM, Figure 2b), high magnification SPIM (20×/0.45 with ~6.5 μm laser-sheet,
147 Figure 2d) and confocal microscope (10×/0.4, Figure 2e). The linecuts through the
148 transverse plane of neuron dendrite (Figure 2a-d) by each method reveal significantly
149 improved resolution from Mars-SPIM, which surpasses both 20×-SPIM result with
150 anisotropic resolution in the longitudinal direction, and Mv-SPIM result with
151 insufficient overall resolution (Figure 2g). With significantly enhanced isotropic
152 resolution, two giant pyramidal neurons across large volume (~400 gigavoxels for
153 entire sample) were finely segmented, as shown in blue and red colors in Figure 2f and
154 g. We note that, besides the increased space-bandwidth product (volume size divided
155 by resolution)[4,5], Mars-SPIM also shows an improvement of signal-to-noise ratio
156 (SNR), which can help to discern the weak signals from strong background of thick

tissue (Supplementary Figure 7). Furthermore, we test different number of views to verify that 8 views fight a good balance between the data size/throughput and performance (Supplementary Figure 8). Mars-SPIM thus can be considered as a light-sheet microscope that is less vulnerable to spherical aberration and light scattering in thick tissue, and combines the large FOV and high-resolution advantages which are difficult to be both met in previous methods. From another perspective, its stitching-free, continuously scanning mode exhibits a higher acquisition throughput as well as lower photobleaching than those stitching-based methods. In Figure 2h, we rate the imaging performance of standard 4× SPIM, 20× SPIM, 10× Confocal and our 4× Mars-SPIM through comparing their system complexity, imaging speed, photo-bleaching rate, and spatial resolution (also see Supplementary Figure 9 and supplementary table 1). Compared to the confocal microscope (10×), the Mars-SPIM gains an advantage in the imaging depth and axial resolution (Supplementary Figure 10 and 11). Besides the well-balanced volumetric resolution, the Mars-SPIM yields a highest effective throughput at ~400 gigavoxels SBP by 20 minutes' acquisition. Mars-SPIM also eliminates the need of mechanical stitching, slicing, high-maintenance optics, and precisely-modulated illumination, using a relatively simple light-sheet setup and fast GPU-based computation to address the general challenge of high-throughput, high-resolution 3-D microscopy that is originally coupled to the physical limitation of system's optics. In the following whole-brain applications, this underlying robustness allows Mars-SPIM prototype to image the entire thick organ at high spatial-temporal performance while keep a simple set-up.

179

180 **High-throughput, *intoto* imaging of whole mouse brain at high resolution**

181 A 8-weeks whole mouse brain (*Tg*: *thy1-GFP-M*) was optically cleared by A-uDISCO
182 method[39], before being imaged by Mars-SPIM. The size of brain shrank from
183 ~9.3*14*7.1 mm to ~7*9.5*5 mm (Figure 3a). Despite the use of tissue clearing, light
184 attenuation/scattering from the deep remains a big challenge to the complete imaging
185 of whole brain (Supplementary Figure 13). On the other hand, brain-wide biomedical
186 applications such as cell population mapping and neuronal projection tracing,
187 intrinsically need high spatial resolution across large area, hence highlighting the
188 significance of Mars-SPIM method. Experimentally, the whole brain was imaged under
189 a low-magnification setup of 25 μm light-sheet illumination plus ×2.2 wide-field
190 detection, and thereby was only required to be stitched twice due to the large FOV. Then
191 the brain was rotated for each view of nonaxial scan (950 nm step-size, 5500 frames in
192 110 s), with totally 16 views of raw stacks rapidly obtained in around half an hour.
193 Following abovementioned SVR-MVD procedure, we successfully reconstructed the
194 entire brain with an isotropic voxel size of 0.975 μm. Figure 3b shows the reconstructed
195 volume rendering of the whole brain (400 gigavoxels, MIP mode). The horizontal
196 planes (x-y) at different depths (Figure 3c-e) and coronal planes (x-z) at different
197 heights (Figure 3f-h) are extracted from the reconstructed brain volume and compared
198 to the conventional SPIM results. It's obvious that Mars-SPIM shows remarkable
199 improvements in resolution, contrast, and signal integrality. The vignette high-
200 resolution Mars volumes of five selected areas (Figure 4a), including the left and right

201 cortex, hippocampus, thalamus and cerebellum, are shown in Figure 4b-f, respectively.
202 The strong efficacy of neural signal recovery as well as resolution enhancement by
203 Mars-SPIM are further illustrated in Supplementary Figure 13, in which a full coronal
204 plane by conventional SPIM that experiences strong scattering from both illumination
205 (x) and emission (z) is compared with the same plane by Mars-SPIM. With quickly
206 creating cellular-resolution brain atlas that encompasses 400 gigavoxels across an over
207 300 $mm^3$ large volume (post-computation time ~12 hours), Mars-SPIM enables high-
208 throughput analysis of massive neurons at whole brain level, which are otherwise
209 spatially or temporally more challenging to regular light sheet microscopes. (Figure 2h,
210 Supplementary Figure 14).
211

212 **Whole-brain visualization and segmentation**

213 Based on the Mars-SPIM reconstruction of whole brain (8-weeks mouse), we explored
214 the neuron cyto-structures at various brain sub-regions and precisely traced the
215 interregional long-distance projection of neurons, which is crucial for understanding
216 the functionality of brain (Figure 5, Supplementary Video 3, 4 and 5). After Mars-SPIM
217 reconstruction of the whole brain, we used an adaptive registration method[40-42] to three-
218 dimensionally map the brain to standard Allen Brain Atlas (ABA). The brain was first
219 re-orientated from horizontal view to coronal view and pre-aligned to ABA
220 automatically using Elastix. This pre-aligned brain was then resized into LR and HR
221 groups respectively, as shown in Figure 5a, step 2. Next, we finely registered the LR
222 group to ABA, and obtained the transform correspondence (step 3) which was further

223 applied to the HR group to obtain a registered-and-transformed HR brain (step 4). This
224 mapped brain atlas was finally visualized in Imaris for follow-up neuron analysis
225 (Figure 5a).

226 With creating the atlas, the neurons localized at different encephalic regions, such
227 as cortex, hippocampus, cerebellum and midbrain, could be identified (Figure 5b) and
228 *intoto* mapped out at whole-brain scale (Figure 5c). Then the neuron population as well
229 as density in different encephalic regions were quantified via calculating the volume of
230 the regions and counting the identified cell bodies within them (Figure 5d). The result
231 shows that among the 12 primary regions, hippocampus formation has the highest
232 neuron density of 4600 cells/mm$^3$, which is consistent with the prior knowledge[43]. It is
233 noteworthy that currently the low-number counting results are obtained based on *thy-*
234 *1-GFP-M* transgenic mouse, in which less than 10% of all motor axons, retinal ganglion
235 cells, lumbar dorsal root ganglion, and cortex express GFP signal[44]. According to the
236 registered HR images, we could trace the neuron projection passed through different
237 brain regions. The whole brain data were volumetrically rendered with several sub-
238 regions segmented by different colors. Figure 5e shows the horizontal and coronal
239 views of the volume renderings, respectively. The trajectories of 6 long-distance (LD)
240 projection neurons were successfully traced and annotated in the digital whole-brain,
241 revealing how they broadcast across the different regions of brain (Figure 5f). Given
242 the fact that this quantitative analysis was implemented based on *thy-1-GFP* mouse
243 with a large number of neurons being labeled, this procedure could be more efficient as
244 the mouse brain has been more specifically labeled, e.g., by virus tracer. Through

245 abovementioned demonstration, our strategy has shown its potentials in imaging-based
246 quantifications for whole-brain or other whole-organ-level analysis, which are crucial
247 for a variety of applications in histology, pathology, neuroscience, etc.
248

249 **Discussion**

250 Mars-SPIM can computationally surpass the resolution limit of a regular light-sheet
251 microscope and suppress the light scattering/attenuation often existed in thick tissue
252 imaging. Unlike mechanical slicing and tile stitching that require complicated operation,
253 this strategy provides a simple and efficient way for high-throughput whole brain
254 mapping at single-cell resolution. The use of simple optics in Mars-SPIM offers an
255 ultra-large FOV of hundreds of $mm^3$, for directly coverage of the whole brain (or other
256 whole organs). Its stitching-free, continuous scanning mode greatly reduces the
257 acquisition time from traditionally several hours to several minutes. Corresponding to
258 the rapid data acquisition, a highly GPU-parallelized SVR-MVD computation flow is
259 followed to reconstruct the super-resolved 3-D brain atlas at a high throughput of a few
260 hours. In our demonstration, the quickly reconstructed digital mouse brain by Mars-
261 SPIM presents an isotropic cellular resolution (~2 μm) with three- to ten- folds
262 resolution improvement, as compared to conventional macro-view SPIM. It is also
263 noted that this Mars-SPIM strategy can be applicable to most existing light-sheet
264 microscopes by a simple retrofit, and expand the optical throughput for fast, high-
265 resolution mapping of whole biological specimens without necessarily increasing the
266 system complexity. Thus, it can be characterized as a high-throughput 3-D imaging

method with a simple and cost-effective setup. Furthermore, Mars-SPIM imaging in conjunction with efficient brain registration can form a pipeline for creating isotropic whole-brain atlas, with which brain-wide quantitative analysis, e.g., neuron populations, densities, and long-distance neuronal projections, could be easily implemented. With combing recent advances in specimen preparation techniques, such as fluorescence-friendly tissue clearing, virus-based sparse labelling and transgenic animal models, Mars-SPIM could be more powerful in enabling various cellular analyses of neural systems. Besides the whole-brain mapping, we believe Mars-SPIM method could be the same efficient when imaging other mammalian organs, e.g., lung, kidney, heart, etc., and benefits a variety of biomedical applications. Furthermore, its ability to readily accomplish cellular imaging of mesoscale organisms at hundreds of gigavoxels SBP renders Mars-SPIM a widely applicable tool for cellular profiling, phenotyping, or sample screening assays in histology, pathology, and development biology, in which both large-scale statistics and cellular details are often desired for whole-tissue level study.

# Methods

## Mars-SPIM imaging setup

A fiber-coupled DPSS laser (CNI laser, 488 nm, single-mode fiber) was used for excitation source. The laser was first collimated into a Gaussian beam with diameter ~3.3 mm (Thorlabs, F280FC-A). Then a sandwich structure containing a convex lens (f = 50 mm, Thorlabs, AC254-050-A) and two cylindrical lenses (f = 30 mm and 150

289 mm, Thorlabs, LJ1212L1, LJ1934L1) was designed to transform the round beam into
290 an elliptical shape. The expansion ratio in short (x) and long (y) axis was ×0.6 and ×3,
291 respectively, forming an elliptical beam with size of 10 by 2 mm (Supplementary Figure
292 2). A pair of adjustable mechanical slits (0-8 mm aperture, Thorlabs, VA100C/M) were
293 placed orthogonally to further truncate the beam and thereby tune the height and
294 thickness of the laser-sheet. The modulated elliptical beam was equally split into two
295 parts via a 50/50 prism (Thorlabs, CCM1-BS014/M), to form two opposite beams,
296 which will be further used to illuminate the sample from dual sides. A dual-side optical
297 sectioning of the whole brain sample was finally formed by using two symmetric
298 combination of cylindrical lens (Thorlabs, LJ1695RM) and illuminating objective
299 (Olympus, 4×/0.10). The laser sheet had a widely tunable range from 5 to 50 μm in
300 thickness and 0.5 to 10 mm in height.
301 Unlike regular detection setup applied in SPIM, we specially used a 4×/0.28 objective
302 in conjunction with an ED Plan 1× tube lens to construct an infinity-corrected, wide-
303 field, and large-aperture detection path (equivalent magnification ×2.2). Compared to
304 the conventional infinity-corrected low-magnification detection, e.g, 2× Nikon
305 objective plus 200 mm focal length tube lens, this setup can collect much more
306 fluorescent signals under a large illumination range due to the larger aperture
307 (Supplementary Figure S9). A four-degree-of-freedom motorized stage (x, y, z
308 translation and rotation around the y-axis, Thorlabs and Phidgets Inc.) integrated with
309 a pair of customized tilting plates (10° inclined surface) was constructed for sample
310 mounting , rotating at multiple angle of views, and scanning across the laser sheet in an

311 off-detection-axis direction (Supplementary Figure S1). A digital camera (Hamamatsu
312 Orca Flash 4.0 v2 plus, or Andor Zyla 5.5) continuously records the images from the
313 consecutively illuminated planes at a high speed up to 50 full frames per second.
314

315 **Sample preparation**

316 Tissue clearing is an essential procedure before imaging. Here we used A-uDISCO
317 method to clear the brains of 8-weeks *thy1- GFP* mice (line M, Jackson Laboratory).
318 In the brain block experiment, to preserve the fluorescence and avoid photobleaching,
319 the cleared brain was embedded into a specific formulated resin[45], the refractive index
320 of which was equal to the index-matched immersion. For conducting bead-based
321 registration, fluorescent beads (Lumisphere, 1%w/v, 500 nm, $SiO_2$) were mixed around
322 the sample in the resin. 10 μl of bead stock solution was centrifuged at 1200 rpm for 3
323 minutes with the water-phase supernatant being removed and replaced with 20 μl
324 methanol. Then the methanol-based bead solution was mixed into the resin to form
325 the bead-resin mixture, which was finally poured into a tube mold with the brain
326 specimen embedded. The tube containing beads, resin and sample was stored in a dark
327 place for 2-3 days till it was solidified for LSFM imaging. For the cell body-based
328 registration of brain block, the sample was directly embedded in the resin without the
329 procedure of mixing bead. For whole brain imaging, the brain was dissected with
330 keeping an ~5 mm long spinal cord (Figure 3a). After optical clearing, the sample could
331 be mounted to the stage via connecting the harden spinal cord with the beam shaft of
332 the rotating motor (Figure 3a).

333

334 **Multi-view imaging acquisition**

335 The brain samples were scanned under eight views. Each times of scanning was
336 executed along a non-axial direction with a step-size significantly smaller than the
337 thickness of light sheet. Under continuous scanning mode, this value was determined
338 by the scanning velocity and camera frame rate, varying from 0.3 μm (for brain block)
339 to 1 μm (for whole brain), depending on the optical configuration. The corresponding
340 acquisition time for total 8 views was around 20 and 30 minutes, respectively. The high
341 magnification SPIM images for comparison were obtained using 20× objective plus a
342 thinner light sheet of ~6.5 μm. Finally, hundreds of gigabyte raw images were
343 transferred to a high-capacity SSD RAID of the workstation via the camera link cable.

344

345 **SVR-MVD reconstruction**

346 SVR computation combined multi-view Bayesian deconvolution[38] was implemented to
347 achieve isotropic high-resolution reconstruction of whole mouse brain. Under each
348 view, a series of low-resolution image stacks were extracted from the oversampled raw
349 data[37]. All low-resolution stacks were correlated with each other in term of sub-voxel-
350 resolution displacements and spatially registered to a high-resolution image stack with
351 an oblique, sub-voxel shift. The multiple low-resolution images and an initial guess of
352 high-resolution image were input into a maximum-likelihood-estimation based
353 computation model to iteratively obtain a converged high-resolution image. This high-
354 resolution estimate was corrected into the final reconstruction by a voxel re-alignment,

355 which recovers the accurate shape of the sample. In practice, the SVR algorithm was
356 applied in parallel to quickly obtain resolution-enhanced results for all the views.
357 After SVR processing for each view, the resolution-enhanced results were regarded as
358 input for multi-view reconstruction in Fiji program. Similar with the bead-based
359 registration method[33], here the neuron cell bodies were recognized as fiducial makers
360 to establish the correspondences between each two views. Then all the SVR views
361 could be precisely registered using these correspondences. A multi-view Bayesian
362 deconvolution[33] was applied at the final step to rationally gather the information from
363 all the registered SVR views, and generate an output image with containing complete
364 sample information as well as enhanced isotropic resolution. An improved Richardson-
365 Lucy deconvolution was used to obtain the final deconvolved image with faster
366 convergence. Furthermore, this SVR-MVD computation procedure could be highly
367 parallelized with GPU-based acceleration. The whole processing time for an entire
368 brain atlas (400 gigavoxels) was ~12 hours on a workstation equipped with dual E5-
369 2630 CPU, quad Geforce 1080Ti GPU and 1T memory. This time consumption could
370 be further reduced with employing more powerful computation units.
371

372 **Confocal microscope and UltraMicroscope imaging**

373 The confocal images are taken by Olympus FV3000 under 10× objective, with a voxel
374 size of 0.8 × 0.8 × 2 μm at 0.5 Hz (Supplementary figure 9, 10 and 11). The whole brain
375 images taken by commercial light-sheet microscope (UltraMicroscope, LaVision
376 BioTec) are acquired at 1.6× and 8× magnification, which take about 20 minutes and

450 minutes, respectively (Supplementary figure 14).

**Software**

The synchronization of scanning and acquisition was accomplished by LabVIEW (National Instruments). The SVR processing was implemented by customized code and computed with CUDA acceleration. The multi-view registration was processed in Fiji. The planar x-z planes of PSFs were performed using ImageJ. The 3-D rendering of PSFs were visualized by Amira (Visage Imaging). The visualizations of neuron imaging, including planar projections, 3-D renderings, neuron tracing, were performed by Imaris (Bitplane).

## Acknowledgements

We thank Yongsheng Zhang and Weilin Zeng for technical assistance. We thank Shangbang Gao, Luoying Zhang, Haohong Li, Man Jiang, Bo Xiong for discussions and comments on the manuscript, Yunyun Han for the discussion on the imaging and brain visualization. This work was supported by the National Key R&D program of China (2017YFA0700501, D.Z. and P.F.), the National Natural Science Foundation of China (21874052 for P.F., 61860206009 for D.Z.), the Innovation Fund of WNLO (P.F. and D.Z.) and the Junior Thousand Talents Program of China (P.F.).

## Author contributions

P.F. initiated the investigation, designed the project. J.N., S.L., Y.P., T.Y., and F.Z.

developed the programs, carried out the imaging experiments and implemented quantifications. Y.L., W.M. and T.Y. prepared the samples and helped to analyze the data. P.F., D.Z., and S.Z. contributed, refined the concept and wrote the paper.

## Additional information

Correspondence and requests for materials should be addressed to P.F. at feipeng@hust.edu.cn (P.F.) or D.Z. at dwanzh@hust.edu.cn (S.G.).

## Conflict of interest

The authors declare that they have no conflict of interest.

## References

1 Miyamichi, K. *et al.* Cortical representations of olfactory input by trans-synaptic tracing. *Nature* **472**, 191-196 (2011).

2 Lichtman, J. W. & Denk, W. The big and the small: challenges of imaging the brain's circuits. *Science* **334**, 618-623 (2011).

3 Lohmann, A. W., Dorsch, R. G., Mendlovic, D., Ferreira, C. & Zalevsky, Z. Space–bandwidth product of optical signals and systems. *JOSA A* **13**, 470-473 (1996).

4 Mendlovic, D. & Lohmann, A. W. Space–bandwidth product adaptation and its application to superresolution: fundamentals. *JOSA A* **14**, 558-562 (1997).

5 Greenbaum, A. *et al.* Increased space-bandwidth product in pixel super-resolved lensfree on-chip microscopy. *Scientific reports* **3**, 1717 (2013).

6 Mayerich, D., Abbott, L. & McCormick, B. Knife-edge scanning microscopy for imaging and reconstruction of three-dimensional anatomical structures of the mouse brain. *Journal of microscopy* **231**, 134-143 (2008).

7 Webb, R. H. Confocal optical microscopy. *Reports on Progress in Physics* **59**, 427 (1996).

8 Helmchen, F. & Denk, W. Deep tissue two-photon microscopy. *Nature methods* **2**, 932-940 (2005).

9 Svoboda, K. & Yasuda, R. Principles of two-photon excitation microscopy and its applications to neuroscience. *Neuron* **50**, 823-839, doi:10.1016/j.neuron.2006.05.019 (2006).

10 Nikolenko, V., Poskanzer, K. E. & Yuste, R. Two-photon photostimulation and imaging of neural circuits. *Nature methods* **4**, 943-950 (2007).

11 Katona, G. *et al.* Fast two-photon in vivo imaging with three-dimensional random-access scanning in large tissue volumes. *Nature methods* **9**, 201-208 (2012).

12 Economo, M. N. *et al.* A platform for brain-wide imaging and reconstruction of individual neurons. *Elife* **5** (2016).

13 Gong, H. *et al.* Continuously tracing brain-wide long-distance axonal projections in mice at a one-micron voxel resolution. *Neuroimage* **74**, 87-98 (2013).

14 Gong, H. *et al.* High-throughput dual-colour precision imaging for brain-wide connectome with cytoarchitectonic landmarks at the cellular level. *Nature communications* **7** (2016).

15 Quan, T. *et al.* NeuroGPS-Tree: automatic reconstruction of large-scale neuronal populations with dense neurites. *Nature methods* **13**, 51-54 (2016).

16 Huisken, J., Swoger, J., Del Bene, F., Wittbrodt, J. & Stelzer, E. H. Optical sectioning deep inside live embryos by selective plane illumination microscopy. *Science* **305**, 1007-1009 (2004).

17 Keller, P. J., Schmidt, A. D., Wittbrodt, J. & Stelzer, E. H. Reconstruction of zebrafish early embryonic development by scanned light sheet microscopy. *science* **322**, 1065-1069 (2008).

18 Planchon, T. A. *et al.* Rapid three-dimensional isotropic imaging of living cells using Bessel beam plane illumination. *Nat Methods* **8**, 417-423, doi:10.1038/nmeth.1586 (2011).

19 Schmid, B. *et al.* High-speed panoramic light-sheet microscopy reveals global endodermal cell dynamics. *Nature communications* **4**, 2207, doi:10.1038/ncomms3207 (2013).

20 Keller, P. J., Ahrens, M. B. & Freeman, J. Light-sheet imaging for systems neuroscience. *nature methods* **12**, 27-29 (2015).

21 Guan, Z. *et al.* Compact plane illumination plugin device to enable light sheet fluorescence imaging of multi-cellular organisms on an inverted wide-field microscope. *Biomedical optics express* **7**, 194-208 (2016).

22 Lee, J. *et al.* 4-Dimensional light-sheet microscopy to elucidate shear stress modulation of cardiac trabeculation. *The Journal of clinical investigation* **126**, 1679 (2016).

23 Ertürk, A. *et al.* Three-dimensional imaging of solvent-cleared organs using 3DISCO. *Nature protocols* **7**, 1983-1995 (2012).

24 Hama, H. *et al.* ScaleS: an optical clearing palette for biological imaging. *Nature neuroscience* **18**, 1518-1529 (2015).

25 Tainaka, K. *et al.* Whole-body imaging with single-cell resolution by tissue decolorization. *Cell* **159**, 911-924 (2014).

26 Dodt, H.-U. *et al.* Ultramicroscopy: three-dimensional visualization of neuronal networks in the whole mouse brain. *Nature methods* **4**, 331 (2007).

27 Susaki, E. A. *et al.* Advanced CUBIC protocols for whole-brain and whole-body clearing and imaging. *Nature protocols* **10**, 1709-1727 (2015).

28 Tomer, R., Ye, L., Hsueh, B. & Deisseroth, K. Advanced CLARITY for rapid and high-resolution imaging of intact tissues. *Nature protocols* **9**, 1682-1697 (2014).

29 Pan, C. *et al.* Shrinkage-mediated imaging of entire organs and organisms using uDISCO. *Nature Methods* (2016).

30 Cai, R. *et al.* Panoptic imaging of transparent mice reveals whole-body neuronal projections and skull–meninges connections. Report No. 1546-1726, (Nature Publishing Group, 2018).

31 Swoger, J., Verveer, P., Greger, K., Huisken, J. & Stelzer, E. H. Multi-view image fusion improves resolution in three-dimensional microscopy. *Optics express* **15**, 8029-8042 (2007).

32 Krzic, U., Gunther, S., Saunders, T. E., Streichan, S. J. & Hufnagel, L. Multiview light-sheet

475 microscope for rapid in toto imaging. *Nature methods* **9**, 730-733 (2012).
476 33 Preibisch, S., Saalfeld, S., Schindelin, J. & Tomancak, P. Software for bead-based registration
477 of selective plane illumination microscopy data. *Nature methods* **7**, 418-419 (2010).
478 34 Tomer, R., Khairy, K., Amat, F. & Keller, P. J. Quantitative high-speed imaging of entire
479 developing embryos with simultaneous multiview light-sheet microscopy. *Nature methods* **9**,
480 755-763 (2012).
481 35 Chhetri, R. K. *et al.* Whole-animal functional and developmental imaging with isotropic spatial
482 resolution. *Nat Methods* **12**, 1171-1178, doi:10.1038/nmeth.3632 (2015).
483 36 Liu, S. *et al.* Three-dimensional, isotropic imaging of mouse brain using multi-view
484 deconvolution light sheet microscopy. *Journal of Innovative Optical Health Sciences* **10**,
485 1743006 (2017).
486 37 Fei, P. *et al.* Subvoxel light-sheet microscopy for high-resolution high-throughput volumetric
487 imaging of large biomedical specimens. *Advanced Photonics* **1**, 016002 (2019).
488 38 Preibisch, S. *et al.* Efficient Bayesian-based multiview deconvolution. *nature methods* **11**, 645-
489 648 (2014).
490 39 Li, Y., Xu, J., Wan, P., Yu, T. & Zhu, D. Optimization of GFP fluorescence preservation by
491 modified uDISCO clearing protocol. *Frontiers in neuroanatomy* **12**, 67 (2018).
492 40 Klein, S., Staring, M., Murphy, K., Viergever, M. A. & Pluim, J. P. Elastix: a toolbox for
493 intensity-based medical image registration. *IEEE transactions on medical imaging* **29**, 196-205
494 (2010).
495 41 Renier, N. *et al.* Mapping of brain activity by automated volume analysis of immediate early
496 genes. *Cell* **165**, 1789-1802 (2016).
497 42 Yang, X. *et al.* High-throughput light sheet tomography platform for automated fast imaging of
498 whole mouse brain. *Journal of biophotonics* **11**, e201800047 (2018).
499 43 Murakami, T. C. *et al.* A three-dimensional single-cell-resolution whole-brain atlas using
500 CUBIC-X expansion microscopy and tissue clearing. *Nature neuroscience* **21**, 625 (2018).
501 44 Feng, G. *et al.* Imaging neuronal subsets in transgenic mice expressing multiple spectral variants
502 of GFP. *Neuron* **28**, 41-51 (2000).
503 45 Becker, K. *et al.* Reduction of photo bleaching and long term archiving of chemically cleared
504 GFP-expressing mouse brains. *PloS one* **9**, e114149 (2014).

505

506

# Figures and Captions

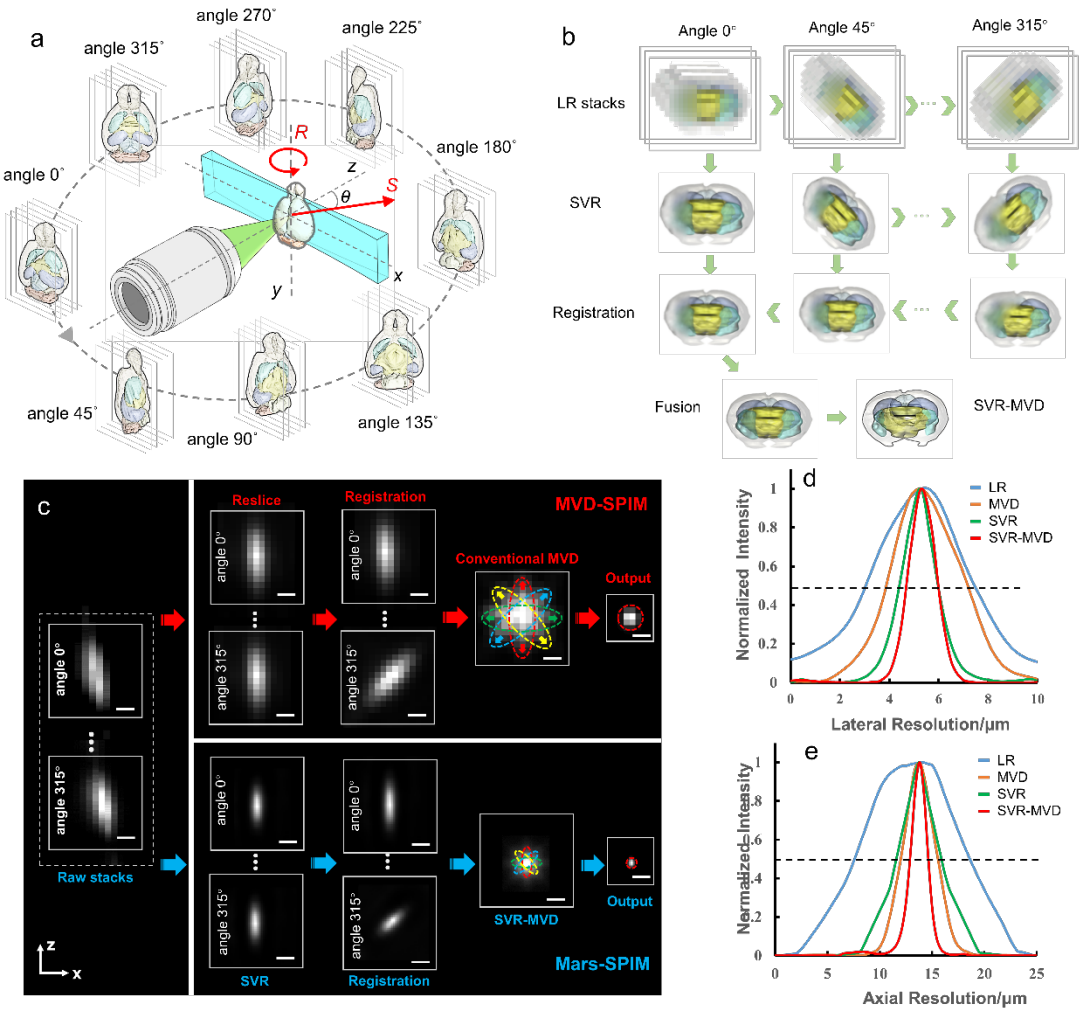


**Figure 1. Illustration and characterization of Mars-SPIM. (a)** The schematic of Mars-SPIM. A low NA objective generates a relatively thick light-sheet and a low magnification objective collects fluorescence with large FOV. The operation of the sample includes four degrees of freedom as: x axis, y axis, non-axial direction s and rotation (along y axis). Unlike standard z-scan SPIM, here the 3-D scanning vector s (red) has a certain angle θ with respect to the x, y, z axes. This off-z-axis scanning strategy in conjunction with a small step size encrypts the raw image stack with lateral and axial sub-voxel-size shifts, which can be used to reconstruct a resolution-enhanced volumetric image via SVR procedure. To suppress the light scattering from the deep tissues and achieve isotropic 3-D resolution, the whole brain sample is rotated and imaged under eight views. **(b)** The

work flow of SVR-MVD procedure which can *intoto* reconstruct the whole brain at isotropically enhanced resolution. It majorly includes: first, the SVR computation for multi-view, sub-voxel-scanned raw images; second, feature-based registration of SVR-processed images; and third, a Bayesian-based deconvolution that generates the final output based on multi-view SVR images. **(c)** The resolution comparison between single-view raw image, SVR only, MVD only and SVR-MVD, via resolving sub-resolution fluorescent beads (~500 nm diameter). x-z images show the lateral and axial extents of the resolved beads (red circles). **(d)-(e)** The intensity plots of the linecuts through the resolved beads along the lateral and axial directions, respectively. The SVR-MVD shows an obviously highest isotropic resolution at ~1.4 μm, which is compared to ~4.2 (lateral) and 12 μm (axial) in raw image. Scale bars: 5 μm in **(c)**.

530

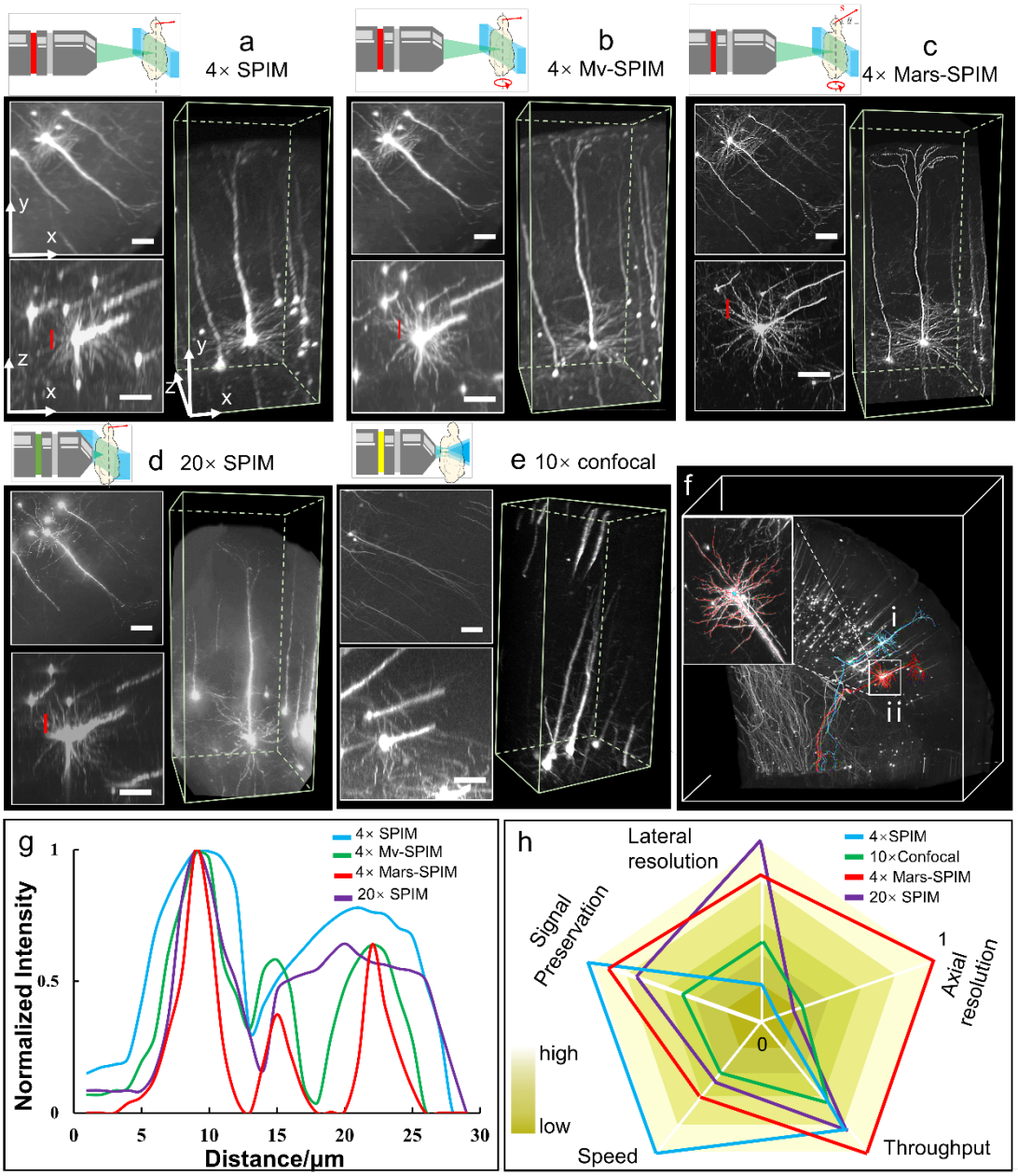


531

532 **Figure 2. Mars-SPIM demonstration on *thy1-GFP* brain block. (a)** Visualization of the neurons

533 at cortex area by conventional SPIM using 4×/0.28 objective plus a 15 μm laser-sheet. The voxel

534 size is 1.625 by 1.625 by 6 μm. **(b)** Conventional multiview SPIM (Mv-SPIM) results with an

535 isotropic voxel size of 1.625*1.625*1.625 μm. **(c)** The Mars-SPIM results of the same neurons, with

536 an isotropic reconstructed voxel size of 0.41*0.41*0.41 μm. **(d)** Comparison from high-resolution

537 SPIM using 20×/0.45 air objective plus 6.5 μm light-sheet. Due to the increasing spherical

aberration under higher magnification, the SNR of the images is obviously decreased. **(e)** The intensity plot of the dash lines transversely across a few neural fibers in **(a) - (d)**. It shows Mars-SPIM has the narrowest peaks which indicate highest resolving power in practice. **(f)** The SVR-MVD reconstruction of the entire brain block with size around 3 by 3 by 3 mm. As a result of finer reconstruction, two pyramidal neurons with dendrites and axons are finely segmented, shown as (**i**) and **(ii)**. (**g**) Vignette high-resolution view of the segmented neuron (**ii**) in **(f)**, showing the clearly resolved fibers. **(h)** The radar map that compares the system simplicity, imaging throughput, photo-bleaching, and spatial resolutions of four methods. The values are outputted by the logarithm and normalized. Scale bars are 50 μm in **(a)-(e)**.

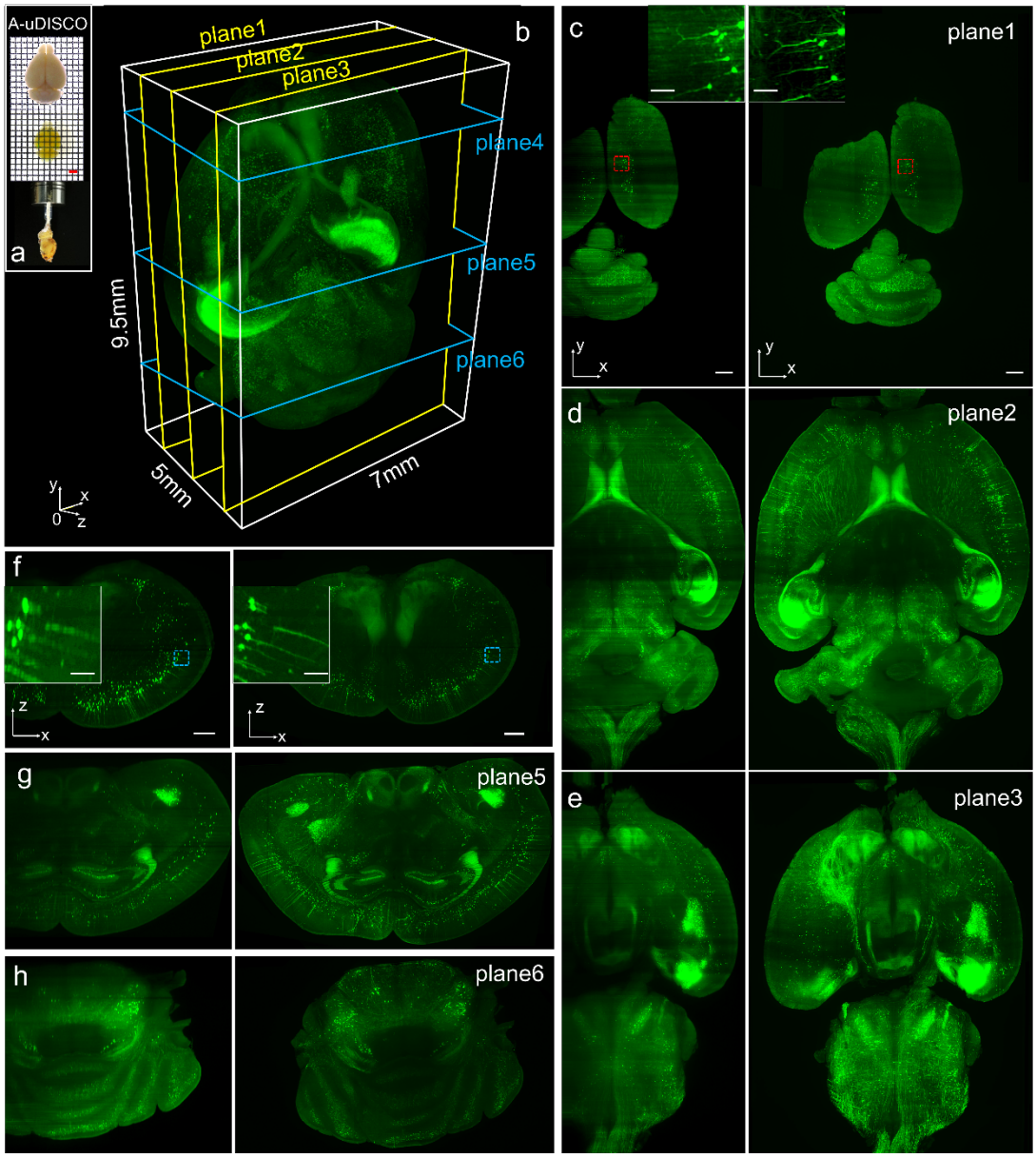


**Figure 3. Comparison of whole mouse brain image by conventional SPIM and Mars-SPIM.** **(a)** The photographs of an adult mouse brain (8 weeks) before and after A-uDISCO clearing. **(b)** The 3D reconstruction of cleared whole mouse brain. With obtaining optically cleared brain for light-sheet imaging, our Mars-SPIM system rapidly provides 3D visualization of entire brain via SVR-MVD reconstruction (400 gigavoxels). Under each view, the sample is imaged using 2.2× magnification plus ~25 μm laser-sheet. The sub-voxel scanning step size is ~1 μm. The final result is recovered from raw images of eight views, with reconstructed isotropic voxel size of 1 by 1 by 1

μm. The imaging throughput here is ~30 minutes per whole brain, and the post-processing time is ~12 hours with employing quad NVIDIA graphical cards. **(c)-(e)** compare the transverse (xy) planes at 500, 2500 and 4000 μm z-depth, by conventional SPIM and Mars-SPIM. Mar-SPIM shows more uniform image quality at the deep of tissue. **(f)-(h)** correspondingly compare the reconstructed coronal (xz) planes at the height of 1500, 4000 and 8000 μm. The completely blurred parts by tissue scattering/attenuation are discarded in conventional SPIM images. Besides the reconstruction integrity of whole brain, the insets in **(c)-(e)** and **(f)-(g)** further compares the achieved lateral and axial resolutions of regular SPIM images and Mars-SPIM images with using the same optics. Scale bars: 500 μm in **(b)-(g)** and 100 μm in insets.

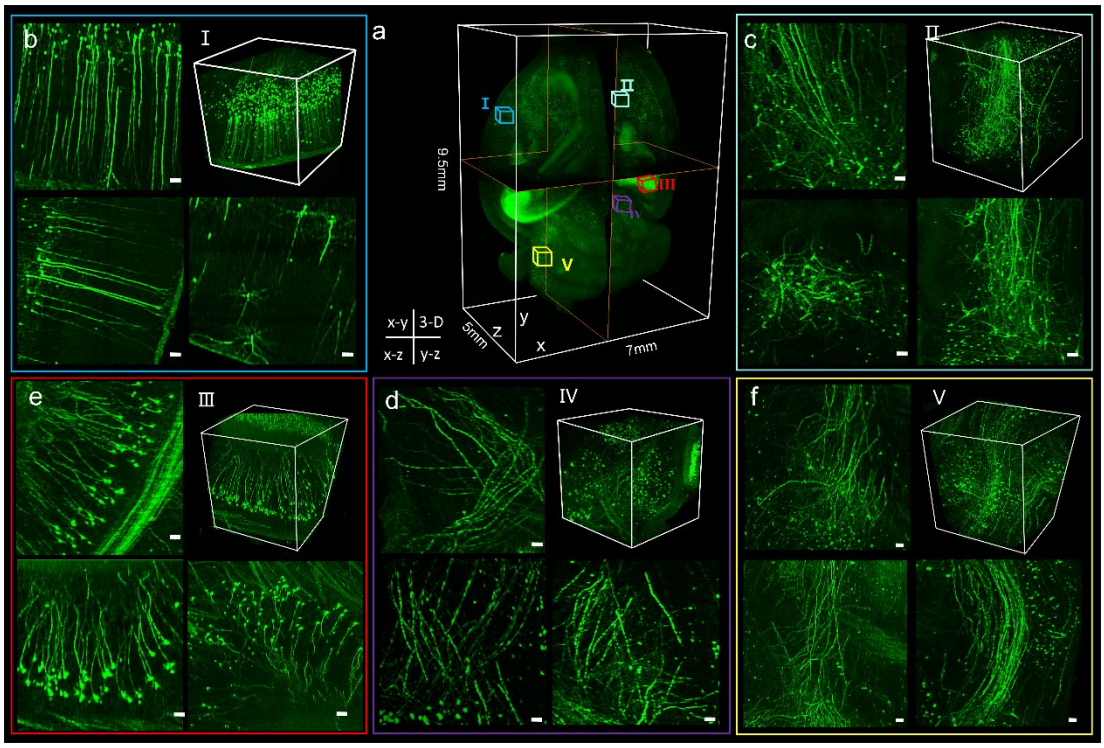


**Figure 4. High-throughput, whole-brain imaging at isotropic cellular resolution using Mars-SPIM. (a)** The reconstructed whole mouse brain by Mars-SPIM. Five selected volumes **(I-V)** at left cortex (blue), right cortex (cyan), hippocampus (red), thalamus (purple) and cerebellum (yellow) are shown in **(b)-(f)**, respectively, with each one containing the transverse (x-y), sagittal (y-z), coronal (x-z) planes and 3-D rendering of the selected volume. The neuronal cell bodies together with the projecting fibers can be identified as a result of significantly enhanced resolutions by Mars-SPIM. Scale bars: 20 μm in **(b)-(f)**.

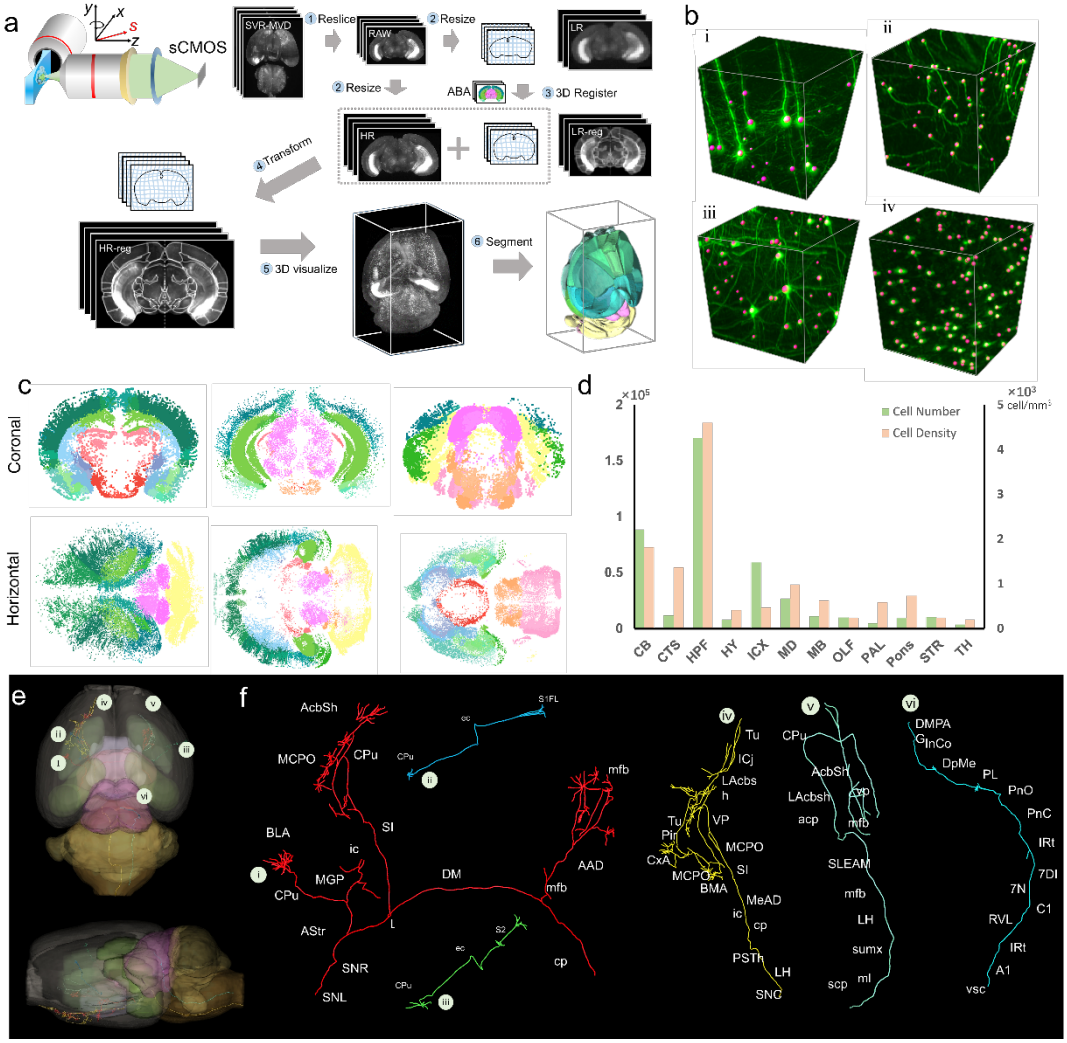


578

579 **Figure 5. Quantifications of a *thy1-GFP-M* mouse brain based on Mars-SPIM image. (a)** The

580 quick creation of whole brain atlas. Step 1: re-orientation of the Mars-SPIM image from horizontal

581 to coronal view and pre-alignment to standard Allen brain atlas (ABA) using Elastix. Step 2: resizing

582 the pre-aligned coronal images into low-resolution (LR) and high-resolution (HR) groups. Step 3:

583 registration of LR group to ABA to obtain the transformation matrix. Step 4: Application of the

584 transformation matrix to HR group to obtain the registered HR images. Step 5: 3D visualization of

585 the ABA-registered brain. Step 6: Segmentation of the brain regions in Amira. **(b)** With isotropic

586 single-cell resolution at whole-brain scale, 3D detection of single neurons can be readily achieved

587 at various brain regions. As a result, the neuron distribution at different regions of the whole brain

588 can be mapped out, as shown in the coronal and transverse views in (c). Each color represents a
589 brain region. **(d)** The neuron population and density calculated at 12 primary brain regions. CB,
590 cerebellum; CTS, cortical subplate; HPF, hippocampal formation; HY, hypothalamus; ICX,
591 isocortex; MD, medulla; MB, midbrain; OFL, Olfactory areas; PAL, pallidum; Pons, pons; STR,
592 striatum; TH, thalamus. **(e)** Horizontal and coronal views of the traced neuron long-distance
593 projections shown in volumetric rendering. **(f)** The pathway annotations of 6 long-distance
594 projection neurons. Abbreviations: AAD, anterior amygdaloid area, dorsal part; Acbsh, accumbens
595 nucleus, shell; Astr, amygdalostriatal transition area; BLA, basolateral amygdaloid nucleus, anterior
596 part; cp, CPu, caudate putamen (striatum); DM, ic, LH, lateral hypothalamic area; MCPO,
597 magnocellular preoptic nucleus; mfb, medial forebrain bundle; MGP, medial globus pallidus
598 (entopeduncular nucleus); SI SNL, substantia nigra, lateral part; SNR, substantia nigra, reticular
599 part; Tu, olfactory tubercle; ICj, islands of Calleja; LAcbsh, lateral amygdaloid nucleus; VP, ventral
600 pallidum; Pir, piriform cortex; CxA, cortex-amygdala transition zone; MCPO, magnocellular
601 preoptic nucleus; SI, substantia innominate; BMA, basomedial amygdaloid nucleus, anterior part;
602 MeAD, medial amygdaloid nucleus, anterior dorsal; ic, internal capsule; cp, cerebral peduncle, basal
603 part; PSTh, parasubthalamic nucleus; LH, lateral hypothalamic area; SNC, substantia nigra,
604 compact part; vsc, ventral spinocerebellar tract; A1, A1 noradrenaline cells; IRt, intermediate
605 reticular nucleus; RVL, rostroventrolateral reticular nucleus; C1, C1 adrenaline cells; 7N, facial
606 nucleus; 7DI, facial nucleus, dorsal intermediate subnucleus; PnC, pontine reticular nucleus, caudal
607 part; PnO, pontine reticular nucleus, oral part; PL, paralemniscal nucleus; DpMe, deep
608 mesencephalic nucleus; InCo, intercollicular nucleus; DMPAG, dorsomedial periaqueductal gray;
609 S1FL, primary somatosensory cortex, forelimb region; CPu, caudate putamen; ec, external capsule;

610 S2, secondary somatosensory cortex; scp, superior cerebellar peduncle; ml, medial lemniscus; sumx,

611 supramammillary decussation; LH, lateral hypothalamic area; mfb, medial forebrain bundle;

612 SLEAM, sublenticular extended amygdala, medial part; acp, anterior commissure, posterior; AcbSh,

613 accumbens nucleus, shell; vp, ventral pallidum;

614